HHS Public Access

Author manuscript

J Comput Aided Mol Des. Author manuscript; available in PMC 2020 November 22.

Published in final edited form as:

J Comput Aided Mol Des. 2019 November ; 33(11): 983–996. doi:10.1007/s10822-019-00246-4.

A_3 Adenosine Receptor Activation Mechanisms: Molecular Dynamics Analysis of Inactive, Active, and Fully Active States

Antonella Ciancetta[*,§], **Priscila Rubio**, **David I. Lieberman**, **Kenneth A. Jacobson**[*]

Molecular Recognition Section, Laboratory of Bioorganic Chemistry, National Institute of Diabetes and Digestive and Kidney Diseases, National Institutes of Health, Bethesda, Maryland 20892 USA.

Abstract

We investigated the Gi-coupled A_3 adenosine receptor (A_3AR) activation mechanism by running 7.2 μs of molecular dynamics (MD) simulations. Based on homology to G protein-coupled receptor (GPCR) structures, three constitutively active mutant (CAM) and the wild-type (WT) A_3ARs in the apo form were modeled. Conformational signatures associated with three different receptor states (inactive R, active R*, and bound to Gi protein mimic) were predicted by analyzing and comparing the CAMs with WT receptor and by considering site-directed mutagenesis data. Detected signatures that were correlated with receptor state included: Persistent salt-bridges involving key charged residues for activation (including a novel, putative ionic lock), rotameric state of conserved $W^{6.48}$, and Na^+ ions and water molecules present. Active-coupled state signatures similar to the X-ray structures of β_2 adrenergic receptor-Gs protein and A_{2A}AR-mini-Gs and the recently solved cryo-EM A_1AR-Gi complexes were found. Our MD analysis suggests that constitutive activation might arise from the $D107^{3.49}$-$R108^{3.50}$ ionic lock destabilization in R and the $D107^{3.49}$-$R111^{3.53}$ ionic lock stabilization in R* that presumably lowers the energy barrier

[*]**Corresponding Authors:** A.Ciancetta@sygnaturediscovery.com (A.C.). Phone: +44 (0)28 9097 2368. kennethj@niddk.nih.gov (K.A.J.). Phone: (+1) 301-496-9024.

[§]Current address: Sygnature Discovery, Nottingham, United Kingdom

Author Contribution

A.C. designed and oversaw the project, run molecular dynamics simulations of the R*G state, analyzed the trajectories, and wrote the manuscript. D. I. L. built the homology and augmented reality models, P. R. performed molecular dynamics simulations of the R and R* states. K. A. J. oversaw the project and wrote the manuscript. All authors have given approval to the final version of the manuscript.

Conflict of interests

The authors declare no conflict interests.

Data Availability

Initial 3D coordinate, topology, parameter, and HTMD protocol files for all the simulated systems are available from the corresponding authors upon request. AR models for selected WT hA3AR R, R*, and R*G conformations compatible with Unity game engine for Microsoft HoloLens (.fbx file format) as well as with other augmented or mixed reality tools (.dae or .obj/.mtl file formats) are available from the authors upon request.

Supplementary Information

Additional modeling information, containing Supplementary Figures S1-S7 and Tables S1-S3 (PDF).

Supplementary Videos S1-S3 (AVI) representing A3AR MD simulations (corresponding to Figures 1 – 3) and Videos S4-S6 (AVI) with HoloLens 3D views of the A3AR (S4, inactive; S5, active; S6, active bound to mini-Gi).

associated with an R to R* transition. This study provides new opportunities to understand the underlying interactions of different receptor states of other Gi protein-coupled GPCRs.

1. INTRODUCTION

The human A_3 adenosine receptor (hA_3AR) is a member of a family of G protein-coupled receptors (GPCRs) activated by adenosine. To date, four AR subtypes have been identified, each of which is characterized by a distinct affinity for the endogenous agonist and tissue distribution [1]. The hA_3AR is expressed at the highest levels in liver, lung and immune cells [2], but lower levels are found in heart and brain and other tissues [3]. From the pharmaceutical perspective, hA_3AR agonists have promising therapeutic potential as anti-inflammatory, anticancer, and cardioprotective agents, with multiple ongoing clinical trials [4–6]. At the cellular level, hA_3AR activation leads to adenylate cyclase (AC) inhibition to reduce cytosolic cyclic AMP (cAMP) levels via a Gi protein (inhibitory guanine nucleotide-binding protein). Among the other AR subtypes, the Gi-coupled hA_1AR shares the highest sequence identity (49%) with the hA_3AR. The other two AR family members, the hA_{2A} and hA_{2B} ARs, principally increase cAMP levels via stimulatory Gs proteins.

In the last two decades, efforts have been devoted to elucidating the structure and activation mechanism of the hA_3AR [7]. Site-directed mutagenesis (SDM) experiments identified key residues involved in ligand binding and receptor activation [8–10]. Specific mutation sites in the conserved DRY motif in transmembrane domain (TM) 3 and in TM6 were found to convert the hA_3AR into constitutively active mutants (CAMs) [9]. The $A229E^{6.34}$ (number in superscript refers to Ballesteros-Weinstein notation [11]), $R108A^{3.50}$, and $R108K^{3.50}$ mutant A_3ARs displayed enhanced agonist-independent activity, while binding agonists with an affinity equal to or greater than the wild-type (WT) receptor [9]. The level of basal cAMP produced in COS-7 cells expressing the CAMs were 69±12, 101±22, and 149±42 pmol/mL, for $A229E^{6.34}$, $R108A^{3.50}$, and $R108K^{3.50}$ mutant hA_3ARs, respectively, to establish the following trend in increased receptor activation with respect to the WT (basal cAMP produced: 256±32 pmol/mL): $A229E^{6.34} > R108A^{3.50} > R108K^{3.50}$ [9]. To rationalize these observations, it was hypothesized that the mutations increase the population of the hA_3AR active state that is able to couple with the Gi protein [9]. However, the lack of a three-dimensional structure of the hA_3AR or of a close homologue GPCR hindered further support for this hypothesis at a detailed atomic level.

Although a hA_3AR structure remains elusive, the progress made in the last decade in structural biology led to X-ray structures of two other AR family members, i.e. the hA_{2A} and the hA_1 ARs. These structures and their sequence homology enable the construction of reliable homology models (HMs) of the hA_3AR [12–23]. In particular, the $hA_{2A}AR$ represents to date the only Class A GPCR that has been solved in the inactive (R) [12,15–17,19,20], active-intermediate (R*) [13], and fully active state coupled to an engineered Gs protein α subunit (R*G) [21]. These structural templates offer the opportunity to model the hA_3AR in different receptor states and study their behavior using modeling techniques such as molecular dynamics (MD).

In this study, we performed 7.2 μs of MD simulations of the hA_3AR by building HMs of the receptor in three different states (R, R* and R*G) and compared the behavior of the three CAMs ($A229E^{6.34}$, $R108A^{3.50}$, and $R108K^{3.50}$) with the WT receptor. The local conformational dynamics analysis of each receptor state enabled us to identify signatures of the inactive, active and active-coupled receptor states that provide a structural framework for the experimental observations and help elucidate at the molecular level the differences between those receptor conformations. As one of the first attempts of MD simulation of a Gi-coupled GPCR system, our study might eventually help understand the intra- and inter-molecular interactions stabilizing different receptor states of other Gi protein-coupled Class A receptors.

2. RESULTS

2.1 Project Design

To identify the signatures of hA_3AR inactive, active and active-coupled states we used different $hA_{2A}AR$ X-ray templates (Figure S1) and built HMs of the both WT and CAM hA_3ARs in the inactive (R), active (R*), and $G\alpha_i$-coupled (R*G) states. To model R, we built a HM based on the high-resolution $hA_{2A}AR$ X-ray structure in the inactive state (PDB ID: 4EIY) [15]. To model the R* and R*G states, we built HMs based on the recently solved $hA_{2A}AR$ X-ray structure in complex with a mini-Gs protein mimicking the Gs protein α subunit (PDB ID: 5G53) [21]. Because parts of the second extracellular loop (EL2) and extracellular (EC) tip of TM1 were not fully resolved in the active X-ray template, we modeled those portions from the inactive $hA_{2A}AR$ X-ray structure (PDB ID: 4EIY) [15], therefore using a hybrid template (Figure S1). The R and R* HMs were subjected to initial validation by computing Ramachandran plots that revealed a few outliers, which were corrected during the equilibration (Figure S2). To model the $G\alpha_i$ coupled to the receptor in the R*G state, we used the engineered mini-Gs protein as template and built a hypothetical "mini-Gi" HM based on the $G\alpha_{i1}$ subunit sequence (sequence alignment in Figure S3). Although this approach represents an approximation, as it was shown that mini-Gi constructs are not stable experimentally [24], trajectory inspection confirmed that the mini-Gi HM did not unfold during the simulation (Figure S4). Moreover, structural comparison between the initial HM and available X-ray structures of the human $G\alpha_i$ subunit (Figure S5) confirmed the overall good superimposition for the modeled construct except for the hgh4 loop region and the N-terminal portion of H4, for which the folding and orientation differed from the $G\alpha_i$ X-ray structures. Notably, the hgh4 loop displayed high B-factor values in the original mini-Gs X-ray template and was oriented toward TM5 and TM6 to presumably interact with the unresolved receptor intracellular loop (IL)3. As it was difficult to discern whether the structural deviation of the hgh4 was attributable to specific $G\alpha_i/G\alpha_s$ structural differences or to the presence of the interacting loop unresolved in the X-ray template, we decided not to refine the initial mini-Gi HM and to restrict our analysis to the immediate A_3AR/mini-Gi protein interface. As shown in Figure S3, the sequence of the modeled mini-Gi is highly conserved in the three $hG\alpha_i$ subtypes. Therefore, our modeling approach, although containing limitations, can provide valuable insights into R*G states of other Gi-coupled receptors.

The available computing resources allowed us to simulate approximately 0.6 μs per system within a reasonable amount of time (~3 weeks/system). By considering the number of HMs and receptor states that we intended to simulate (4 HMs in 3 different states for a total of 12 systems), we performed multiple short simulations (0.2 μs) in triplicate rather than a single, long simulation. It has been recently demonstrated that conclusions drawn from multiple shorter replicates are more reliable than those from a single, longer simulation [25]. Due to the relatively short time simulated, insufficient to detect large-scale TM movements and reorganization, we intentionally did not model the receptor activation as a conversion from the R to the R* state and investigated each receptor state separately. In particular, we analyzed the MD trajectories of the WT R, R*, and R*G states to detect signatures of inactive, active and active-coupled states, respectively, and used them to analyze the CAM simulations. We inspected in detail the differences between R and R* and between R* and R*G states of the receptor by analyzing the variations of: *(i)* salt-bridges persistency (Psb) and H-bond patterns, *(ii)* the rotameric state of the conserved W243$^{6.48}$ residue, *(iii)* the presence of Na^+ ions at the E19$^{1.39}$ and the conserved D58$^{2.50}$ sites, and *(iv)* the TM domain hydration.

The Psb parameter indicates the percent simulated time in which the N-O distance of oppositely charged residues was <4.0 Å. The rotameric state of the conserved W243$^{6.48}$ residue was evaluated by computing the side chain χ_1 and χ_2 values and their corresponding conformations (Figure S6) during the trajectories. The presence of the Na^+ ions was expressed as percent simulated time in which the ion was at a distance < 4.0 Å from the E19$^{1.39}$ and D58$^{2.50}$ side chains. The TM domain hydration was evaluated as the number of water molecules present within the TM bundle. The average Root Mean Square Deviation (RMSD) and Fluctuation (RMSF) of the hA_3AR alpha carbon atoms (Cα) were used to measure model stability and to select a representative trajectory for each system for visualization purposes. All the above mentioned estimates were expressed as average values computed over three independent replicates.

2.2 Analysis of hA3AR Inactive State R

As highlighted in Table 1, the WT receptor in the R state featured four ion-pairs constituting two intrahelical and two interhelical salt-bridges that persisted for > 50% of the simulation time. Electrostatic interactions between two non-conserved residues at the EC tip of TM5 (D175$^{5.30}$-R173$^{5.34}$, Psb: 98±1%), and two highly conserved residues at the IC tip of TM3 (D107$^{3.49}$-R108$^{3.50}$, Psb: 76±12%) formed the two intrahelical salt-bridges. The interhelical salt-bridges, D199$^{5.60}$-K113$^{3.55}$ (Psb: 74±22%) and E225$^{6.30}$-R111$^{3.53}$ (Psb: 76±12%), connected the IC tip of TM3 to TM5 and TM6, respectively. Of the above-mentioned ion-pairs, non-conserved D175$^{5.30}$-R173$^{5.34}$ and D199$^{5.60}$-K113$^{3.55}$ likely represent an intrinsic feature of this receptor, and the conserved D107$^{3.49}$-R108$^{3.50}$ [26] and the novel E225$^{6.30}$-R111$^{3.53}$ salt-bridges presumably stabilize the receptor inactive state (Figure 1A and Video S1). Notably, in a hA_1AR X-ray structure in complex with an antagonist [22], the D$^{5.60}$-K$^{3.55}$ side chains lay close (although not interacting) and the E$^{6.30}$-R$^{3.53}$ pair formed a salt-bridge, therefore suggesting that those are features shared by Gi-coupled ARs. We hypothesize that the E$^{6.30}$-R$^{3.53}$ salt-bridge represents an alternative ionic lock, *i.e.* a salt-bridge locking the receptor in a specific conformation, which is also feasible only in opsin-3

and −5, according to Class A GPCRs structure-based sequence analysis [27]. From the above-described analysis, we therefore identified the presence/persistency of D107$^{3.49}$-R108$^{3.50}$ and E225$^{6.30}$-R111$^{3.53}$ salt-bridges as *inactive state signatures* (Figure 1A) and used them to compare the R state of CAMs to the WT (Video S1).

The conservative R108K mutation negatively impacted the persistency of the inactive state signatures [26], as the E225$^{6.30}$-R111$^{3.53}$ salt-bridge was less persistent with respect to the WT model (Psb: 27±11% vs 54±22 for the R108K and the WT, respectively) and the D107$^{3.49}$-K108$^{3.50}$ salt-bridge (virtually corresponding to the D107$^{3.49}$-R108$^{3.50}$ ion-pair) was not formed. During the MD simulations (Video S1), both the N-O distance and the side chain geometry of those two vicinal residues were not compatible with salt-bridge formation. Instead, the K108$^{3.50}$ faced the IC environment and established a salt-bridge with E225$^{6.30}$ (Figure 1B, Psb: 86±12%), therefore engaging in an alternative ionic lock.

The non-conservative R108A mutation strongly impacted the persistency of both inactive state signatures (Figure 1C and Video S1). The unavailability of a positively charged residue at position 3.50 did not allow the formation of a salt-bridge with the nearby D107$^{3.49}$ residue. Moreover, the E225$^{6.30}$-R111$^{3.53}$ ionic lock persistency was also considerably decreased (Psb: 21±15%).

The non-conservative A229E mutation also decreased the persistency of both inactive state signatures. With respect to the WT model, the D107$^{3.49}$-R108$^{3.50}$ persistency decreased (Psb: 34±9%), while the E225$^{6.30}$-R111$^{3.53}$ ionic lock was not detected. However, as depicted in Figure 1D, the newly introduced E229$^{6.34}$ and R111$^{3.53}$ side chains engaged in a salt-bridge, therefore creating an alternative ionic lock (Psb: 72±26%).

As detailed in Table 2, the CAMs featured average higher Cα RMSD and RMSF values with respect to the WT. As a probable result of a less rigid receptor structure, in the CAMs the TM domain hydration increased by ~6–13% (Table 3). Two Na^+ ions were detected in proximity to the conserved E19$^{1.39}$ and D58$^{2.50}$ side chains (Table 3), and a network of H-bonds involving T46$^{2.38}$, T47$^{2.39}$, and Y118 (a conserved residue in IL2) stabilized the side chain of D107$^{3.49}$ in all the receptors (Video S1). The χ_1/χ_2 angles of W243$^{6.48}$ predominately adopted (trans, gauche) *t/g(−)* conformations, with the exception of the R108K hA_3AR mutant for which the *g(−)/g(−)* conformation predominated (Table 3).

2.3 Analysis of hA3AR Active State, R*

The WT R* state featured a different pattern of salt-bridges with respect to the R state involving residues in the IC tips of TM3, TM5 and TM6 (Table 1). The putative ionic lock E225$^{6.30}$-R111$^{3.53}$ was broken (Psb: 0%), as E225$^{6.30}$ interacted with the conserved (R/K in 43% of class A GPCRs) R205$^{5.66}$ (Psb: 82±10%). The latter salt-bridge was already present in the $hA_{2A}AR$ X-ray template and, according to our MD analysis, helps stabilize the outward displaced TM6. Another characteristic interaction in the WT R* state was an intrahelical salt-bridge connecting D107$^{3.49}$ of the conserved DRY motif and R111$^{3.53}$ (Psb: 69±14%), a residue conserved in Gi-coupled ARs. D107$^{3.49}$-R111$^{3.53}$ formation was favored by the conformational change of R108$^{3.50}$, which faced the α5 subunit of the co-crystallized mini-Gs protein in the X-ray template. Although in the R* model we did not include the Gi

protein mimic, during the MD simulations, the side chain of R108$^{3.50}$ facing the unoccupied IC environment was stabilized by a network of H-bond interactions involving Y107$^{5.58}$ and Y282$^{7.53}$ (Video S2). From the analysis of WT trajectories, we identified the presence/persistency of the D107$^{3.49}$-R111$^{3.53}$ and E225$^{6.30}$-R205$^{5.66}$ salt-bridges as *active state signatures* (Figure 2A).

In the R108K mutant hA$_3$AR (Figure 2B), the persistency of both active state signatures increased. The D107$^{3.49}$-R111$^{3.53}$ and the E225$^{6.30}$-R205$^{5.66}$ salt-bridges were more persistent with respect to the WT model (D107$^{3.49}$-R111$^{3.53}$: 69±14% vs 92±1% for the WT and R108K HMs, respectively; E225$^{6.30}$-R205$^{5.66}$: 82±10 vs 89±9% for the WT and R108K HMs, respectively). During the MD simulations (Video S2), K108$^{3.50}$ faced the IC environment and did not engage in specific interactions with other residues (Table 1).

The R108A mutation (Figure 2C and Video S2) strongly favored D107$^{3.49}$-R111$^{3.53}$ salt-bridge formation (Psb: 96±5%) while decreasing the E225$^{6.30}$-R205$^{5.66}$ salt-bridge persistency.

Analogously to the R108A mutation effect, in the A229E mutant hA AR the D107$^{3.49}$-R111$^{3.53}$ salt-bridge persistency increased, and the E225$^{6.30}$-R205$^{5.66}$ salt-bridge persistency decreased with respect to the WT (Table 1). As emerged from trajectory analysis (Video S2), the availability of an additional charged residue in TM6 favored the formation of an alternative/additional salt-bridge, E229$^{6.34}$-K230$^{6.35}$ (Psb: 44±4%), that competed with the E225$^{6.30}$-R205$^{5.66}$ signature (Figure 2D). As in the WT R* model, the A229E R* mutant receptor featured additional R108$^{3.50}$ side chain stabilization through water-mediated H-bond interactions with the Y107$^{5.58}$ and Y282$^{7.53}$ side chains, although less persistent with respect to the network observed for the WT R* model (Video S2).

The R* CAMs featured average lower Cα RMSD and RMSF values with respect to the WT and to their respective R HMs (Table 2), while increasing by ~6–9% the TM domain hydration with respect to the WT (Table 3) probably as an effect of a more stable opened receptor conformation. All the R* HMs featured a single Na^+ ion residing in proximity to the conserved E19$^{1.39}$ side chain and predominant *g(−)*/*g(−)* conformations for the χ_1/χ_2 angles of conserved W243$^{6.48}$.

2.4 Analysis of the hA$_3$AR Active-Coupled State, R*G

The introduction of the mini-G$_i$ model increased the WT R* hA$_3$AR stability (Cα RMSD$_{ave}$ for the A$_3$AR: 2.71 vs 3.40 Å for the R*G and R* HMs, respectively), although this HM was found to be less stable than in the R state (Cα RMSD$_{ave}$: 1.92 Å). This stabilization was not observed for the CAMs, as their R* states proved to be more stable than the R*G HMs (Table S1 and S2).

In the R*G WT model simulation, the persistency of various active state signatures decreased: the D107$^{3.49}$-R111$^{3.53}$ salt-bridge was absent, and the E225$^{6.30}$-R205$^{5.66}$ salt-bridge persisted for ~56% of the time (Table S1). The inspection of the trajectories highlighted alternative interaction patterns involving the R111$^{3.53}$ side chain, that established H-bond and salt-bridge interactions with N347$^{H5.19}$ (using the CGN notation for

G proteins [28]) and D350$^{H5.22}$ residues located in the α5 segment of the Gα$_i$ model (Figure 3A and Video S3). The D107$^{3.49}$ side chain maintained a persistent H-bond network with T47$^{2.39}$ and Y118 (IL2), that was detected in both R and R* HMs. The MD trajectory analysis of the R*G CAMs (Video S3) showed a variation in the persistency of active state signatures that was dependent upon the specific mutation (Table S2). All three mutants maintained a stable D107$^{3.49}$-R111$^{3.53}$ salt-bridge (Figure 3B–D), although its persistency decreased with respect to the corresponding R* models (Table S1). The E225$^{6.30}$-R205$^{5.66}$ salt-bridge was also more persistent in the R108K and R108A R*G models, whereas in the A229E R*G model it persisted for ~15% of the time due to the competing E229$^{6.34}$-R205$^{5.66}$ salt-bridge formation (Psb: 44±43%).

The Psb analysis at the interface between the WT hA$_3$AR and the Gαi subunit (Table 4) highlighted specific interactions involving residues located in IL2 (K119 and R120), and at the IC tip of TM5 (K207), and IL3/TM6 (K216). Of the above-listed residues, only K119 (IL2) is conserved in A$_1$ and A$_{2B}$ ARs. Along with electrostatic interactions, extended hydrophobic contacts were established involving the IC tips of TM3 and TM5, IL2, and the G$_i$ protein C-terminal domain. The contact surface involved the side chains of R111$^{3.53}$, V112$^{3.54}$, V116 (IL2), Y197$^{5.58}$ I200$^{5.61}$, I203$^{5.64}$, I204$^{5.65}$ and L208$^{5.69}$ of the hA$_3$AR and I343$^{H5.15}$, I344$^{H5.16}$, L348$^{H5.20}$, C351$^{H5.23}$, L353$^{H5.25}$, F354$^{H5.26}$ of the Gα$_i$ subunit.

From the above described analysis, we identified the presence/persistency of salt bridges and hydrophobic contacts at the interface between the hA$_3$AR and the Gα$_i$ subunit as *active-coupled state signatures*. The CAMs showed a general increase in the persistency of salt-bridges (Table S4). In all the MD simulations of the R*G HMs, favorable hydrophobic contacts between residues in the Gα$_i$ subunit C-terminal domain and residues in the hA$_3$AR TM5 and TM6 were detected (transparent surfaces in Video S3).

Similarly to the R* models, the R*G HMs featured one Na^+ ion in proximity to the conserved E19$^{1.39}$ side chain and predominant *g(−)*/*g(−)* conformations for the χ_1/χ_2 angles of W243$^{6.48}$ (Table S3). The TM hydration increased by ~20–30% with respect to the R state HMs, but only modestly and not consistently with respect to the R* models (Table S3 and S7).

3. Discussion

Recent progress in structural biology has led to the determination of X-ray structures of several class A GPCRs in complex with the Gs protein [29] or an engineered minimal Gsα subunit [21]. Those structures represent valuable templates to model the fully active state (R*G) of homologous GPCRs and to study their conformational states through modeling techniques, such as MD. In this study, we modeled the WT hA$_3$AR and three known CAMs in the R, R*, and R*G states by using the hA$_{2A}$AR X-ray structures in different states as templates. Gaining insight into receptor active and G-protein coupled states and their comparison with the inactive state can aid the design of novel hA$_3$AR agonists. Such agonists could be useful for the treatment of various conditions, including pain, cancer and inflammation [4,6]. This analysis can also help understand the molecular signatures characterizing constitutive active mutants and help in designing engineered receptors by

suggesting new mutation sites that can be validated experimentally and hopefully provide atomistic details that can accelerate the hA_3AR structure determination.

Initiating the MD analysis from different receptor states enabled us to run multiple short simulations (0.2 μs in triplicate for each receptor model/state), thus enhancing the statistical significance of the trajectory analysis and making a comparison with the experimental data more reliable. Moreover, analyzing the dynamic behavior of each receptor state separately allowed us to identify specific signatures pertaining to the considered state. Hence, we derived signatures of inactive, active, and active-coupled states from the analysis of R, R*, and R*G states, respectively (Figures 4 and S6). The notion of specific signatures determining distinct receptor states arises from a large body of evidence identifying the charged residues in the conserved DRY motif (TM3) and $E/D^{6.30}$ as implicated in receptor activation [26,30]. In particular, the formation of specific salt-bridges designated as “ionic locks” has been proposed as a means for GPCRs to maintain an inactive state, although a great variability was observed in the X-ray structures solved to date [31]. Very recently, the analysis of GPCR X-ray structures coupled to different signaling proteins has shed light on commonalities and similarities at the coupling interface [32]. Phylogenetic analysis of human G proteins has identified “selectivity barcodes” in G proteins sequences that are uniquely recognized by GPCRs [33].

From the WT hA_3AR R state MD analysis we identified the presence/persistency of $D107^{3.49}$-$R108^{3.50}$ and $E225^{6.30}$-$R111^{3.53}$ salt-bridges as *inactive state signatures*. In the CAMs the persistency of these signatures was generally decreased. The mutant receptors displayed a different pattern of salt-bridges at the interface between TM3 and TM6: the $D107^{3.49}$-$R108^{3.50}$ inactive state signature persistency was significantly compromised in CAMs involving the conserved DRY motif, *i.e.* the $R108K^{3.50}$ and $R108A^{3.50}$ mutant A_3ARs; the $E225^{6.30}$-$R111^{3.53}$ signature was more impacted in the MD simulation of the $A229E^{6.34}$ mutant A_3AR, due to the formation of an alternative salt-bridge involving the newly introduced negatively charged residue that perturbed the local environment of $E225^{6.30}$. The alternative ionic locks detected in the R state CAMs are presumably not as efficient as the proper inactive state signatures in maintaining the receptor in the inactive state, as the mutant hA_3ARs were found to be generally less stable (average higher Cα RMSD and RMSF values, Table2) than the WT receptor.

From the WT R* state analysis we identified persistent $D107^{3.49}$-$R111^{3.53}$ and $E225^{6.30}$-$R205^{5.66}$ salt-bridges as *active state signatures*. In the CAMs, the $D107^{3.49}$-$R111^{3.53}$ salt-bridge persistency increased. Notably, this active state signature was already detected, although with lower persistency and a great inter-replicate variability, for the R108K (Psb: 26±46%) and R108A (Psb: 38±48%) mutant hA_3ARs in the R state. The $E225^{6.30}$-$R205^{5.66}$ salt-bridge, on the other hand, was subjected to higher variability among the CAMs. The A229E mutant hA_3AR featured an additional interhelical salt-bridge ($E229^{6.34}$-$K230^{6.35}$, Psb: 44±4%). Altogether, the different interaction networks presumably contributed to stabilize the mutant hA_3AR R* states, as they featured average lower Cα RMSD values with respect to both the WT and their respective R states (Table 2).

These observations, together with the experimental evidence showing a higher degree of activation for the A229E mutant hA_3AR [9] suggest that the active R* state stabilization might play a major role in the constitutive hA_3AR activation with respect to the inactive R state destabilization. Our analysis also suggests that a less rigid structure resulting from the R108K, R108A, and A229E point mutations enables a more conspicuous flow of water molecules through the TM bundle (~6–10% increase in the TM domain hydration with respect to the WT for both the R and R* CAMs, Table 3 and S7), which is believed to initiate or be characteristic of GPCR activation[34]. Water molecules stabilized the $R108^{3.50}$ side chain in the MD simulations of the WT and A229E R* states by mediating H-bonds with the $Y197^{5.58}$ and $Y282^{7.53}$ side chains. This interaction pattern was detected in the X-ray structure of a CAM metarhodopsin-II in complex with a Gα subunit C-terminal fragment [35] and stabilized the G protein binding site.

The comparison between the R and R* states revealed two striking differences concerning *(i)* the presence of Na^+ ions in proximity to conserved negatively charged residues in TM1 and TM2, and *(ii)* the $W243^{6.48}$ side chain rotameric state. In the MD simulation of the R states two Na^+ ions persisted in proximity to the conserved sites, interacting with the $E19^{1.39}$ and the $D58^{2.50}$ side chains, respectively. Consistently with the known negative GPCR allosteric modulation of Na^+ binding at the conserved $D^{2.50}$ residue, during the MD simulation of the R* states the $D58^{2.50}$ site was unoccupied. On the other hand, a Na^+ ion was found in proximity to the $E19^{1.39}$ side chain. Hence, our MD analysis suggests that the presence of a Na^+ ion in proximity to the $E19^{1.39}$ side chain does not correlate with the receptor state. However, as we simulated the receptors in the apo form, its relationship to receptor-bound orthosteric ligands has yet to be determined. A more in-depth trajectory analysis revealed that the Na^+ presence at the $E19^{1.39}$ site correlated with the motion at the EC tips of TM1 and TM7 and that the conserved $H272^{7.43}$ residue participated, directly or indirectly, in its coordination (visual inspection, data not shown). SDM studies on the A_{2A} and A_1 ARs implicated $E^{1.39}$ in agonist binding and receptor activation, and its association with $H^{7.43}$ was hypothesized [36,37]. A subsequent study by Gao et al. [38] investigating the role of $E^{1.39}N$ and $H^{7.43}Y$ mutations in receptor regulation by Na^+ ions concluded that these mutation effects were less pronounced compared to the well-characterized allosteric modulation by the $D^{2.50}$ residue with Na^+ ions present [15]. It was suggested that an interaction between $E^{1.39}$ and $H^{7.43}$ might favor a receptor conformation that binds agonist with higher affinity [38]. $A_{2A}AR$ MD studies investigated the possibility of a direct interaction between the $E^{1.39}$ and $H^{7.43}$ side chains and concluded that, for an interaction to occur, $H^{7.43}$ must be protonated [39]. In our simulations, the $H272^{7.43}$ side chain was modeled as neutral with a hydrogen on the N^{δ}, and a Na^+ ion, therefore, mediating the interaction with the $E^{1.39}$ residue. However, it has to be verified if such an interaction pattern is compatible with a nucleoside agonist bound to the receptor, as the $H272^{7.43}$ side chain is predicted to establish a H-bond with the ribose C2' hydroxyl group. Very recently, the free energy profile and binding kinetics of Na^+ ions in several class A and B GPCRs have been investigated by means of kinetic Monte Carlo simulations [40]. The authors suggested that negatively charged residues in EL2 recognize the Na^+ ions approaching the receptors from the extracellular medium. Residues at the interface with TM1 (including $E^{1.39}$) and TM7 were hypothesized to form a putative meta-binding site for the ions before their diffusion to

the conserved $D^{2.50}$ allosteric binding site. For class A GPCRs, the Na^+ ion diffusion was associated with a $W243^{6.48}$ rotameric switch (belonging to the highly conserved CWxP motif).

Interestingly, we also detected different preferences for $W243^{6.48}$ side chain χ_1/χ_2 angles that correlated with the receptor states. Specifically, the *t/g(−)* conformer predominated in the R state, whereas in the R* state the *g(−)/g(−)* conformer was preferred. The $W243^{6.48}$ side chain was subjected to higher fluctuations in the inactive state and the MD simulations of the R108A mutant hA_3AR, therefore suggesting that changes in the interaction pattern at the interface between TM3 and TM6 might trigger this microswitch [31]. To date, the role of the aromatic$^{6.48}$ side-chain in GPCR activation is still a matter of debate [31]. It was early considered an activation microswitch, following spectroscopic evidence revealing changes in the residue environment upon rhodopsin activation [41.42]. However, as this switch has not yet been observed in the X-ray structures of active GPCRs, except the active-intermediate neurotensin receptor structures [43], its involvement in receptor activation has been questioned. On the other hand, it has to be emphasized that early hA_3AR SDM data showed that the $W243^{6.48}$A/F mutations impaired agonist-mediated receptor activation, while not affecting agonist binding [10]. A subsequent study confirmed the critical role of this residue in A_3AR activation and reported changes in agonist efficacy and signaling bias for the $W243^{6.48}$F A_3AR mutant [44]. In line with these experimental observations, both docking and MD studies on hA_3AR HMs based on different templates reported $W243^{6.48}$ side chain conformational changes dependent on the receptor state [45–47]. In addition, MD studies performed on other class A GPCRs, thereby surveying a variety of X-ray structures and models, highlighted conformational changes involving the conserved $W^{6.48}$ side chain [48–50]. It is conceivable that the receptor state in which this conformational change occurs represents a transient species that might be difficult to observe experimentally. In support to this hypothesis, very recently, NMR studies in solution and X-ray crystallographic studies of the $hA_{2A}AR$ and its mutant receptors detected major conformational changes in proximity to $W^{6.48}$ between inactive and active-like states [51,52].

The *active-coupled state signatures* detected from the interaction analysis at the receptor/$G\alpha_i$ subunit interface in WT R*G involved residues located in IL2, and at the IC tip of TM5 and IL3/TM6. The most persistent salt-bridges were the $K207^{5.68}$-$D341^{DG.H5.13}$ and $R120^{IL2}$-$D193^{DG.s2s3.02}$ ionic locks. Extended hydrophobic contacts connected the IC tips of TM3 and TM5, and the G_i protein C-terminal domain. Although the MD analysis of the CAM R*G states showed a general increase in the persistency of both activation and active-coupled state signatures, the salt-bridges displayed a greater inter-replicate variability (Table S4) and depended more on the specific mutation considered, making it difficult to draw general conclusions. It is therefore conceivable that the coupling interface might vary from the WT to the CAM hA_3ARs and, probably due to the approximation introduced by the mini-Gi HM, this variation could not be correctly predicted in our HMs.

In conclusion, we have sampled local conformational dynamics to identify hA_3AR inactive, activate and active-coupled state signatures and investigated the effects of CAMs and a Gi protein mimic on those signatures. Our MD analysis suggests that constitutive activation might arise from the $D107^{3.49}$-$R108^{3.50}$ ionic lock destabilization in R and the $D107^{3.49}$-

R111$^{3.53}$ ionic lock stabilization in R* that presumably lowers the energy barrier associated with an R to R* transition. Furthermore, constitutive activation might also imply that other interactions stabilize the R*G state through salt-bridges (Figures 4 and S6) and favorable hydrophobic contacts. Notably, while this manuscript was in preparation, a cryo-EM structure of the hA_1AR in complex with the Gi protein was solved (PDB ID: 6D9H) [53] featuring three among the activation and active-coupled state signatures here hypothesized for the A_3AR: (i) the D$^{3.49}$-R$^{3.53}$ ionic lock, (ii) a K213$^{5.71}$-D341$^{DG.H5.13}$ salt-bridge virtually corresponding to the K207$^{5.68}$-D341$^{DG.H5.13}$ interaction in the A_3AR, and (iii) the R$^{3.53}$-D350$^{G.H5.22}$ salt-bridge that, although not persistently, was observed in the simulation of the WT A_3AR (Figure 3).

Our study establishes the basis for further investigation of residues implicated in stabilizing the inactive and active states of other related Gi-coupled GPCRs, which hopefully will enhance our understanding of receptor structure and function.

4. Methods

Protein preparation.

To model the receptor inactive state (R), we buitda homology model based on the high-resolution hA_{2A}AR X-ray structure in complex with an antagonist (PDB ID: 4EIY). To model the receptor active (R*) and G protein-coupled fully active (R*G) states, we built a hA_3AR homology model based on the hA_{2A}AR X-ray structure in complex with an agonist and coupled to the engineered mini-Gs protein (PDB ID: 5G53). As in the X-ray template EL2 was not fully resolved, we modeled this portion from the high-resolution antagonist-bound hA_{2A}AR X-ray structure (PDB ID: 4EIY). The template structures were retrieved from the RCSB Protein Data Bank (PDB) [54] (http://www.rcsb.org), and the FASTA sequences of the hA_3AR (Uniprot ID: P0DMS8) and the human Gi protein α_i subunit (Uniprot ID: P63096) were retrieved from the UniProt database [55]. The HMs were built with Prime (Schrödinger, Inc.) by using the knowledge-based method and the ClustalW alignment, which was manually refined (Figure S1). Domains and portions of the G protein absent in the X-ray template (i. e. the N-term alpha helix and the whole helical domain) were not modeled, whereas missing loop regions where reconstructed using the default loop modelling protocol as embedded in Prime. The models were prepared with the Protein Preparation Wizard tool implemented in the Schrödinger suite [56] by optimizing hydrogen atoms (OPLS3 force field, 0.30 Å convergence criterion for heavy atoms RMSD). The histidine protonation states were determined according to H-bond patterns with surrounding residues and solvent exposure as follows: His272$^{7.43}$/322$^{G.S6.4}$ were protonated on the N$^{\delta}$; His195$^{G.S3.2}$/188$^{G.S2.5}$ were doubly protonated, and all the other His residues were protonated on the N$^{\varepsilon}$. After the WT HM preparation, CAMs were built by mutating specific sites with the Mutate Residues tool implemented in Maestro.

Molecular Dynamics.

MD system setup, equilibration, and production were automatized by exploiting the HTMD [57] module (Acellera, Barcelona Spain, version 1.9.4). The HMs were embedded into an 80 × 80 Å (R and R* states) or a 90 × 90 Å (R*G state) 1-palmitoyl-2-oleoyl-*sn*-glycero-3-

phosphocholine (POPC) membrane leaflet generated through the VMD Membrane Plugin tool [58]. Overlapping lipids (within 0.6 Å) were removed upon protein insertion, and the systems were solvated with TIP3P [59] water and neutralized by Na^+/Cl^- counter-ions that were added to reach a final physiological concentration of 0.154 M. The approximate total number of atoms for each model was: ~72,000 atoms (R and R*), and ~127,000 (R*G). MD simulations with periodic boundary conditions were carried out with ACEMD (Acellera, version 2016.10.27) [60] using the CHARMM36 [61,62] force field and a cubic box extending on the z axis by at least 20 Å from protein atoms. The systems were equilibrated through a 5000-step minimization followed by 40 ns of MD simulation in the NPT ensemble by applying initial constrains (0.85 for alpha carbon atoms, and 0.40 for the other protein atoms) that were linearly reduced after 20 ns. During the equilibration, the temperature was maintained at 310 K using a Langevin thermostat with a low damping constant of 1 ps^{-1}, and the pressure was maintained at 1 atm using a Berendensen barostat. Bond lengths involving hydrogen atoms were constrained using the M-SHAKE [63] algorithm. The equilibrated system was subjected to 200 ns of unrestrained MD simulation run in triplicate (NVT ensemble, timestep = 2 fs, damping constant = 0.1 ps^{-1}). Long-range Coulombic interactions were handled using the particle mesh Ewald summation method (PME) [64] with grid size rounded to the approximate integer value of cell wall dimensions. A non-bonded cutoff distance of 9 Å with a switching distance of 7.5 Å was used.

The simulations were run in part on an in-house built cluster equipped with three 970, two 980Ti, and one 1080 NVIDIA GTX GPUs (Nvidia, Santa Clara, CA) and in part by exploiting the High-performance computational capabilities of the Biowulf Linux GPU cluster at the National Institutes of Health, Bethesda, MD (http://biowulf.nih.gov).

MD Trajectory Analysis.

MD trajectory analysis was performed with in-house bash and tcl scripts exploiting the RMSD trajectory (RSMDTT) and the Salt Bridge plugins implemented in VMD [58]. Selection of a representative trajectory for each model/mutant was based on average Cα RMSD. Salt-bridge persistency (Psb) was previously defined [65] as the percent total simulation time in which the N-O distance of each identified pair of oppositely charged residues was < 4.0 Å. Na^+ persistency was expressed as percent simulated time in which a Na^+ ion was within a distance < 4.0 Å from the $E19^{1.39}$ and $D58^{2.50}$ side chains. $W243^{6.48}$ rotameric state was evaluated by computing the side chain χ_1 and χ_2 values and expressing the percent simulated time in which the corresponding conformations were adopted (Figure S6). TM domain hydration was evaluated as the number of water molecules present within the TM bundle by using the hydrophobic tail of the lipid molecules (C21 atoms of POPC residues) as membrane boundaries. All the above-mentioned quantities were expressed as average values computed over three independent replicates. Structures in Figures 1–3 represent the middle structures of the most populated clusters of selected trajectories (indicated in bold in Table 2). Cluster analysis was performed with GROMACS [66] (v 5.1.2) using the GROMOS clustering algorithm and a RMSD cutoff of 2.0 Å.

Augmented Reality Models.

The selected hA_3AR WT conformations (R, R* and R*G) displayed in panel A of Figures 1–3 were rendered as augmented reality (AR) models as follows: the protein representations were exported as Wavefront files (.obj/.mtl) using VMD [58] (v. 1.9.3) and an in-house tcl script. The so-obtained 3D models were post-processed using Blender (v. 2.79.0) through an in-house python script to yield the final .fbx AR models (Figure S8), that were imported and inspected using the Unity game engine (v. 2017.1.3f1) for HoloLens [67] (see Video S4–S6 for a demos). These static views represent the most populated conformation of the selected trajectory for each receptor state (highlighted in bold in Table 2).

Supplementary Material

Refer to Web version on PubMed Central for supplementary material.

Acknowledgements

This research was supported by the National Institutes of Health NIDDK Intramural Research Program (ZIADK031117 and ZIADK031126), the 2017 NIH Summer Mentor Award (A.C.), and the Community College Summer Enrichment Program (P.R.).

References

1. Fredholm BB, IJzerman AP, Jacobson KA, Linden J, Müller CE (2011) International union of basic and clinical pharmacology. LXXXI. Nomenclature and classification of adenosine receptors—An update. Pharmacol. Rev 63:1–34 [PubMed: 21303899]
2. Linden J (1994) Cloned adenosine A_3 receptors: pharmacological properties, species differences and receptor functions. Trends Pharmacol. Sci 15:298–306 [PubMed: 7940998]
3. Lopes LV, Rebola N, Pinheiro PC, Richardson PJ, Oliveira CR, Cunha RA (2003) Adenosine A_3 receptors are located in neurons of the rat hippocampus. Neuroreport 14:1645–1648 [PubMed: 14502093]
4. Jacobson KA, Merighi S, Varani K, Borea PA, Baraldi S, Tabrizi MA, Romagnoli R, Baraldi PG, Ciancetta A, Tosh DK, Gao Z-G, Gessi S (2017) A_3 adenosine receptors as modulators of inflammation: From medicinal chemistry to therapy. Med Res Rev 38:1031–1072. [PubMed: 28682469]
5. Janes K, Symons-Liguori A, Jacobson KA, Salvemini D (2016) Identification of A_3 adenosine receptor agonists as novel non-narcotic analgesics: A_3 receptor agonists as non-narcotic analgesics. Br J Pharmacol 173:1253–1267 [PubMed: 26804983]
6. Fishman P, Bar-Yehuda S, Liang BT, Jacobson KA (2012) Pharmacological and therapeutic effects of A_3 adenosine receptor agonists. Drug Discov Today 17:359–366 [PubMed: 22033198]
7. Ciancetta A, Jacobson KA (2017) Structural probing and molecular modeling of the A_3 adenosine receptor: A focus on agonist binding. Molecules 22:449.
8. Gao ZG, Kim SK, Gross AS, Chen A, Blaustein JB, Jacobson KA (2003) Identification of essential residues involved in the allosteric modulation of the human A_3 adenosine receptor. Mol Pharmacol 63:1021–1031 [PubMed: 12695530]
9. Chen A, Gao Z-G, Barak D, Liang BT, Jacobson KA (2001) Constitutive activation of A_3 adenosine receptors by site-directed mutagenesis Biochem Biophys Res Commun 28:596–601
10. Gao Z-G, Chen A, Barak D, Kim SK, Müller CE Jacobson KA (2002) Identification by site-directed mutagenesis of residues involved in ligand recognition and activation of the human A_3 adenosine receptor. J Biol Chem 277:19056–19063 [PubMed: 11891221]
11. Ballesteros JA, Weinstein H (1995) Integrated methods for the construction of three dimensional models and computational probing of structure function relations in G protein-coupled receptors. Methods Neurosci 25:366–428.

12. Jaakola VP, Griffith MT, Hanson MA, Cherezov V, Chien EY, Lane JR, IJzerman AP, Stevens RC (2008) The 2.6 angstrom crystal structure of a human A_{2A} adenosine receptor bound to an antagonist. Science 322:1211–1217. [PubMed: 18832607]

13. Xu F, Wu H, Katritch V, Han GW, Jacobson KA, Gao ZG, Cherezov V, Stevens RC (2011) Structure of an agonist-bound human A_{2A} adenosine receptor. Science 332:322–327 [PubMed: 21393508]

14. Lebon G, Warne T, Edwards PC, Bennett K, Langmead CJ, Leslie AG, Tate CG (2011) Agonist-bound adenosine A_{2A} receptor structures reveal common features of GPCR activation. Nature 474:521–525 [PubMed: 21593763]

15. Liu W, Chun E, Thompson AA, Chubukov P, Xu F, Katritch V, Han GW, Roth CB, Heitman LH, IJzerman AP, Cherezov V, Stevens RC (2012) Structural basis for allosteric regulation of GPCRs by sodium ions. Science 337, 232–226 [PubMed: 22798613]

16. Congreve M, Andrews SP, Doré AS, Hollenstein K, Hurrell E, Langmead CJ, Mason JS, Ng IW, Tehan B, Zhukov A, Weir M, Marshall FH (2012) Discovery of 1,2,4-triazine derivatives as adenosine A_{2A} antagonists using structure-based drug design. J Med Chem 55:1898–1903 [PubMed: 22220592]

17. Doré AS, Robertson N, Errey JC, Ng I, Hollenstein K, Tehan B, Hurrell E, Bennett K, Congreve M, Magnani F, Tate CG, Weir M, Marshall FH (2011) Structure of the adenosine A_{2A} receptor in complex with ZM241385 and the xanthines XAC and caffeine. Structure 19:1283–1293 [PubMed: 21885291]

18. Lebon G, Edwards PC, Leslie AWG, Tate CG (2015) Molecular Determinants of CGS21680 binding to the human adenosine A_{2A} receptor. Mol. Pharmacol 87:907–915 [PubMed: 25762024]

19. Hino T, Arakawa T, Iwanari H, Yurugi-Kobayashi T, Ikeda-Suno C, Nakada-Nakura Y, Kusano-Arai O, Weyand S, Shimamura T, Nomura N, Cameron AD, Kobayashi T, Hamakubo T, Iwata S, Murata T (2012) G-protein-coupled receptor inactivation by an allosteric inverse-agonist antibody. Nature 482:237–240 [PubMed: 22286059]

20. Segala E, Guo D, Cheng RK, Bortolato A, Deflorian F, Doré AS, Errey JC, Heitman LH, IJzerman AP, Marshall FH, Cooke RM (2016) Controlling the dissociation of ligands from the adenosine A_{2A} receptor through modulation of salt bridge strength. J. Med. Chem 59, 6470–6479 [PubMed: 27312113]

21. Carpenter B, Nehme R, Warne T, Leslie AGW, Tate CG (2016) Structure of the adenosine A_{2A} receptor bound to an engineered G protein. Nature 536:104–107 [PubMed: 27462812]

22. Glukhova A, Thal DM, Nguyen AT, Vecchio EA, Jörg M, Scammells PJ, May LT, Sexton PM, Christopoulos A (2017) Structure of the adenosine A receptor reveals the basis for subtype selectivity. Cell 168:867–877 [PubMed: 28235198]

23. Cheng RKY, Segala E, Robertson N, Deflorian F, Doré AS, Errey JC, Fiez-Vandal C, Marshall FH, Rooke RM (2017) Structures of human A_1 and A_{2A} adenosine receptors with xanthines reveal determinants of selectivity. Structure 25:1275–1285 [PubMed: 28712806]

24. Nehmé R, Carpenter B, Singhal A, Strege A, Edwards PC, White CF, Du H, Grisshammer R, Tate CG (2017) Mini-G proteins: Novel tools for studying GPCRs in their active conformation. PLoS ONE 12, e0175642 [PubMed: 28426733]

25. Knapp B, Ospina L, Deane CM (2018) Avoiding false positive conclusions in molecular simulation: The importance of replicas. J Chem Theory Comput 11, 6127–6138. doi: 10.1021/acs.jctc.8b00391.

26. Rovati GE, Capra V, Neubig RR (2007) The highly conserved DRY motif of class A G protein-coupled receptors: Beyond the ground state. Mol Pharmacol 71:959–964 [PubMed: 17192495]

27. Isberg V, de Graaf C, Bortolato A, Cherezov V, Katritch V, Marshall FH, Mordalski S, Pin JP, Stevens RC, Vriend G, Gloriam DE (2015) Generic GPCR residue numbers - aligning topology maps while minding the gaps. Trends Pharmacol Sci 36:22–31 [PubMed: 25541108]

28. Flock T, Ravarani CN, Sun D, Venkatakrishnan AJ, Kayikci M, Tate CG, Veprintsev DB, Babu MM (2015) Universal allosteric mechanism for Gα activation by GPCRs. Nature 524:173–179 [PubMed: 26147082]

29. Rasmussen SG, DeVree BT, Zou Y, Kruse AC, Chung KY, Kobilka TS, Thian FS, Chae PS, Pardon E, Calinski D, Mathiesen JM, Shah ST, Lyons JA, Caffrey M, Gellman SH, Steyaert J, Skiniotis G,

Weis WI, Sunahara RK, Kobilka BK (2011) Crystal structure of the β_2 adrenergic receptor–Gs protein complex. Nature 477:549–555 [PubMed: 21772288]

30. Rovati GE, Capra V, Shaw VS, Malik RU, Sivaramakrishnan S, Neubig RR (2017) The DRY motif and the four corners of the cubic ternary complex model. Cellular Signalling 35:16–23 [PubMed: 28347873]
31. Venkatakrishnan AJ, Deupi X, Lebon G, Tate CG, Schertler GF, Babu MM (2013) Molecular signatures of G-protein-coupled receptors. Nature 494:185–194 [PubMed: 23407534]
32. Carpenter B, Tate CG (2017) Active state structures of G protein-coupled receptors highlight the similarities and differences in the G protein and arrestin coupling interfaces. Curr Opin Struct Biol 45: 124–132 [PubMed: 28482214]
33. Flock T, Hauser AS, Lund N, Gloriam DE, Balaji S, Babu MM (2017) Selectivity determinants of GPCR–G-protein binding. Nature 454, 317–322.
34. Yuan S, Filipek S, Palczewski K, Vogel H (2014) Activation of G-protein-coupled receptors correlates with the formation of a continuous internal water pathway. Nature Commun 5:4733 [PubMed: 25203160]
35. Deupi X, Edwards P, Singhal A, Nickle B, Oprina D, Schertler G, Standfuss J (2012) Stabilized G protein binding site in the structure of constitutively active metarhodopsin-II. Proc Natl Acad Sci USA 109:119–124 [PubMed: 22198838]
36. Barbhaiya H, McClain R, IJzerman AP, Rivkees SA (1996) Site-directed mutagenesis of human A1 adenosine receptor: Influences of acidic and hydroxy residues in the first four transmembrane domains on ligand binding. Mol Pharmacol 50:1635–1642 [PubMed: 8967987]
37. IJzerman AP, Von Frijtag Drabbe Künzel JK, Kim J, Jiang Q, Jacobson KA (1996) Site-directed mutagenesis of the human adenosine A_{2A} receptor. Critical involvement of Glu^{13} in agonist recognition. Eur J Pharmacol 310:260–272
38. Gao ZG, Jiang Q, Jacobson KA, IJzerman AP (2000) Site-directed mutagenesis studies of human A_{2A} adenosine receptors. Biochem Pharmacol 60:661–668 [PubMed: 10927024]
39. Rodriguez D, Piñeiro Á, Gutiérrez-de-Téran H (2011) Molecular dynamics simulations reveal insights into key structural elements of adenosine receptors. Biochemistry 50:4194–4208 [PubMed: 21480628]
40. Selvam B, Shamsi Z, Shukla D (2018) Universality of the sodium ion binding mechanism in Class A G-protein-coupled receptors. Angew Chem Int Edit 57:3048–3053
41. Lin SW, Sakmar TP (1996) Specific tryptophan UV-absorbance changes are probes of the transition of rhodopsin to its active state. Biochemistry 35:11149–11159 [PubMed: 8780519]
42. Pope A, Eilers M, Reeves PJ, Smith SO (2014) Amino acid conservation and interactions in rhodopsin: probing receptor activation by NMR spectroscopy. Biochim Biophys Acta 1837:683–693 [PubMed: 24183693]
43. Krumm BE, White JF, Shah P, Grisshammer R (2015) Structural prerequisites for G-protein activation by the neurotensin receptor. Nat Commun 6:7895 [PubMed: 26205105]
44. Stoddart LA, Kellam B, Briddon SJ, Hill SJ (2014) Effect of a toggle switch mutation in TM6 of the human adenosine A_3 receptor on Gi protein-dependent signalling and Gi-independent receptor internalization. Br J Pharmacol 171:3827–3844. [PubMed: 24750014]
45. Hallmen C, Wiese M (2006) Molecular dynamics simulation of the human adenosine A_3 receptor: agonist induced conformational changes of Trp243. J Comput Aided Mol Des 20:673–684 [PubMed: 17124628]
46. Kim SK, Gao ZG, Jeong LS, Jacobson KA (2006) Docking studies of agonists and antagonists suggest an activation pathway of the A_3 adenosine receptor. J Mol Graph Model 25:562–577 [PubMed: 16793299]
47. Kim SK, Riley L, Abrol R, Jacobson KA, Goddard WA (2011) Predicted structures of agonist and antagonist bound complexes of adenosine A_3 receptor. Proteins 79:1878–1897. [PubMed: 21488099]
48. Yuan S, Hu Z, Filipek S, Vogel H (2015) W6.48 opens a gate for a continuous intrinsic water pathway. Angew Chem Int Edit 54:556–559
49. Huang W, Manglik A, Venkatakrishnan AJ, Laeremans T, Feinberg EN, Sanborn AL, Kato HE, Livingston KE, Thorsen TS, Kling RC, Granier S, Gmeiner P, Husbands SM, Traynor JR, Weis

WI, Steyaert J, Dror RO, Kobilka BK (2015) Structural insights into mu-opioid receptor activation. Nature 524:315–321 [PubMed: 26245379]

50. Krumm BE, Lee S, Bhattacharya S, Botos I, White CF, Du H, Vaidehi N, Grisshammer R (2016) Structure and dynamics of a constitutively active neurotensin receptor. Sci Rep 6:38564 [PubMed: 27924846]
51. Eddy MT, Lee M-Y, Gao Z-G, White KL, Didenko T, Horst R, Audet M, Stanczak P, McClary KM, Han GW, Jacobson KA, Stevens RC, Wüthrich K (2018) Allosteric coupling of drug binding and intracellular signaling in the A_{2A} adenosine receptor. Cell 172:68–80. [PubMed: 29290469]
52. White KL, Eddy MT, Gao ZG, Han GW, Lian T, Deary A, Patel N, Jacobson KA, Katritch V, Stevens RC (2018) Structural connection between activation microswitch and allosteric sodium site in GPCR signaling. Structure 26:259–269. [PubMed: 29395784]
53. Draper-Joyce CJ, Khoshouei M, Thal DM, Liang YL, Nguyen ATN, Furness SGB, Venugopal H, Baltos JA, Plitzko JM, Danev R, Baumeister W, May LT, Wootten D, Sexton PM, Glukhova A, Christopoulos A (2018) Structure of the adenosine-bound human adenosine A1receptor-Gi complex. Nature 558:559–563. [PubMed: 29925945]
54. Berman HM, Westbrook J, Feng Z, Gilliland G, Bhat TN, Weissig H, Shindyalov IN, Bourne PE (2000) The Protein Data Bank. Nucleic Acids Research 28:235–242. [PubMed: 10592235]
55. The UniProt Consortium (2017) UniProt: the universal protein knowledgebase. Nucleic Acids Res 45:D158–D169 [PubMed: 27899622]
56. Sastry GM, Adzhigirey M, Day T, Annabhimoju R, Sherman W (2013) Protein and ligand preparation: parameters, protocols, and influence on virtual screening enrichments. J. Comput. Aided Mol Des 27: 221–234 [PubMed: 23579614]
57. Doerr S, Harvey MJ, Noé F, De Fabritiis G (2016) HTMD: High-throughput molecular dynamics for molecular discovery. J Chem Theory Comput 12:1845–1852 [PubMed: 26949976]
58. Humphrey W, Dalke A, Schulten K (1996) VMD - Visual Molecular Dynamics. J Mol Graphics 14:33–38
59. Jorgensen WL, Chandrasekhar J, Madura JD, Impey RW, Klein ML (1983) Comparison of simple potential functions for simulating liquid water. J Chem Phys 79:926–935
60. Harvey M, Giupponi G, De Fabritiis G (2009) ACEMD: Accelerated molecular dynamics simulations in the microseconds timescale. J Chem Theory Comput 5:1632–1639 [PubMed: 26609855]
61. Best RB, Zhu X, Shim J, Lopes PEM, Mittal J, Feig M, MacKerell AD (2012) Optimization of the Additive CHARMM All-Atom Protein Force Field Targeting Improved Sampling of the Backbone Phi, Psi and Side-Chain Chi1 And Chi2 Dihedral Angles. J Chem Theory Comput 8, 3257–3273 [PubMed: 23341755]
62. Klauda JB, Venable RM, Freites JA, O'Connor JW, Tobias DJ, Mondragon-Ramirez C, Vorobyov I, MacKerell AD, Pastor RW (2010) Update of the CHARMM all-atom additive force field for lipids: Validation on six lipid types. J Phys Chem B 114, 7830–7843 [PubMed: 20496934]
63. Kräutler V, Van Gunsteren WF, Hünenberger PH (2001) A Fast SHAKE Algorithm to Solve Distance Constraint Equations for Small Molecules in Molecular Dynamics Simulations. J Comput Chem 22, 501–508
64. Essmann U, Perera L, Berkowitz ML, Darden T, Lee H, Pedersen LGA (1995) Smooth Particle Mesh Ewald Method. J Chem Phys 103, 8577–8593.
65. Ciancetta A, O'Connor RD, Paoletta S, Jacobson KA (2017) Demystifying $P2Y_1$ receptor ligand recognition through docking and molecular dynamics analyses. J Chem Inf Model 57, 3104–3123 [PubMed: 29182323]
66. Hess B, Kutzner C, van der Spoel D, Lindahl E (2008) GROMACS 4: Algorithms for highly efficient, load-balanced, and scalable molecular simulation. J Chem Theory Comput 4, 435–447. [PubMed: 26620784]
67. Wang S, Parsons M, Stone-McLean J, Rogers P, Boyd S, Hoover K, Meruvia-Pastor O, Gong M, Smith A (2017) Augmented Reality as a Telemedicine Platform for Remote Procedural Training. Sensors 17, 2294, doi:10.3390/s17102294.

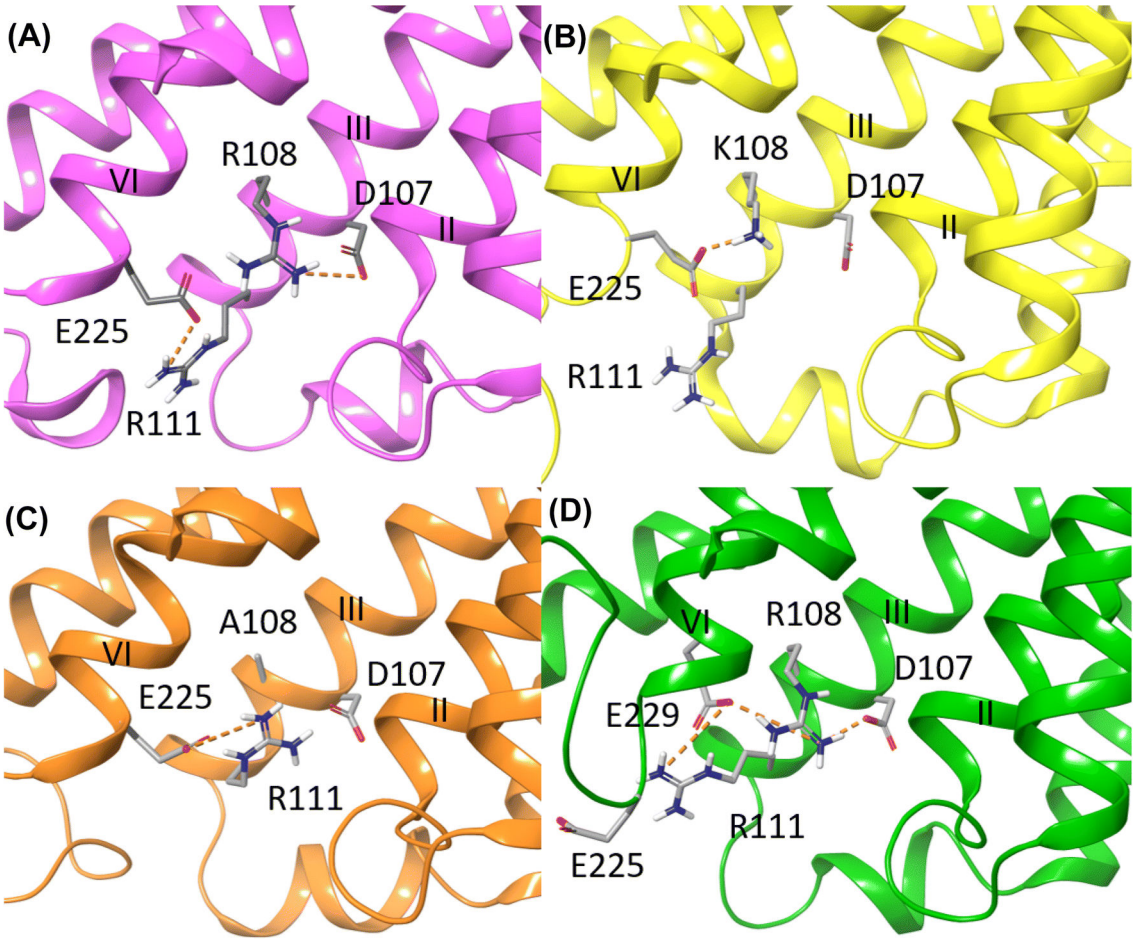

Figure 1.

3D representation of A_3AR inactive state signatures that decreased in CAMs (trajectories shown in video S1). Most persistent salt-bridges (range dashed lines) detected during 0.6 μs of MD simulations of the R HMs. View of the intracellular side of most populated conformations of the A) WT (magenta ribbons), B) R108K (yellow ribbons), C) R108A (orange ribbons), and D) A229E (green ribbons) hA_3ARs. Selected residues (grey carbons, stick representation) and TMs are labeled.

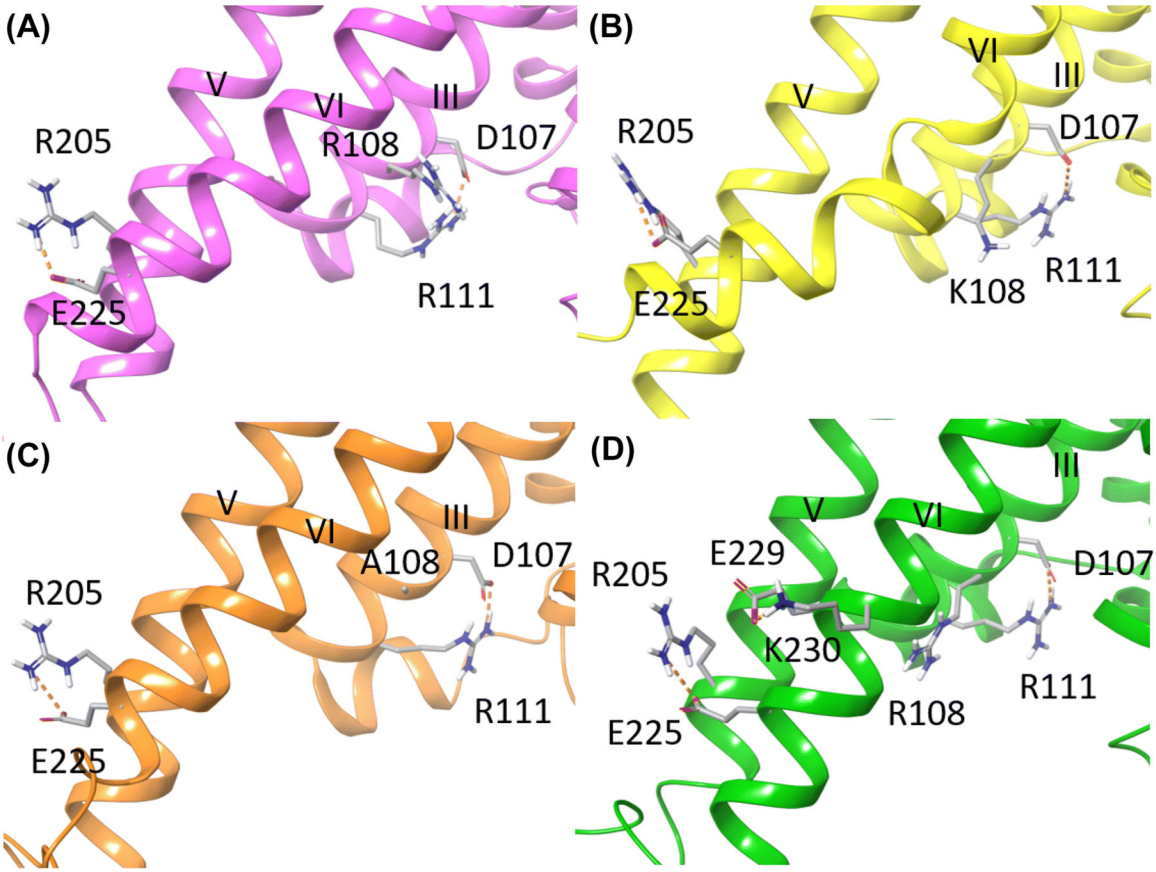

Figure 2.

3D representation of A_3AR active state signatures that increased in CAMs (trajectories shown in video S2). Most persistent salt-bridges (orange dashed lines) detected during 0.6 μs of MD simulations of the R* HMs. View of the intracellular side of most populated conformations of the A) WT (magenta ribbons), B) R108K (yellow ribbons), C) R108A (orange ribbons), and D) A229E (green ribbons) hA_3ARs. Selected residues (grey carbons, stick representation) and TMs are labeled.

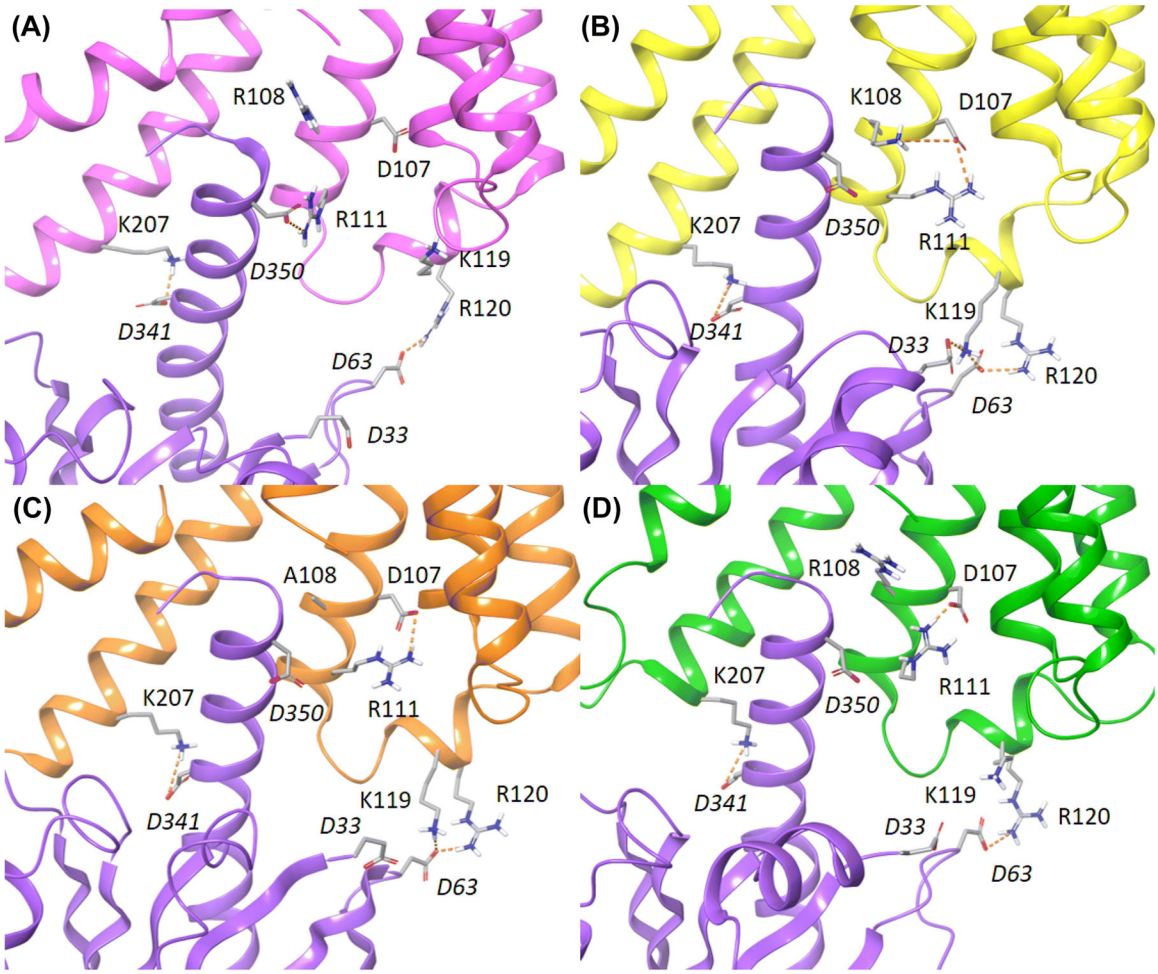

Figure 3.

Active-coupled state signatures of A_3AR that increased in a hypothetic complex with mini-Gi (trajectories shown in video S3). Most persistent salt-bridges (orange dashed lines) detected during 0.6 μs of MD simulations of the R*G HMs. View of the intracellular side of most populated conformations of the A) WT (magenta ribbons), B) R108K (yellow ribbons), C) R108A (orange ribbons), and D) A229E (green ribbons) hA_3ARs. The $G\alpha_i$ subunit is represented as purple ribbons. Selected residues (grey carbons, stick representation) are labeled. Residues belonging to the $G\alpha_i$ subunit are labeled in italics.

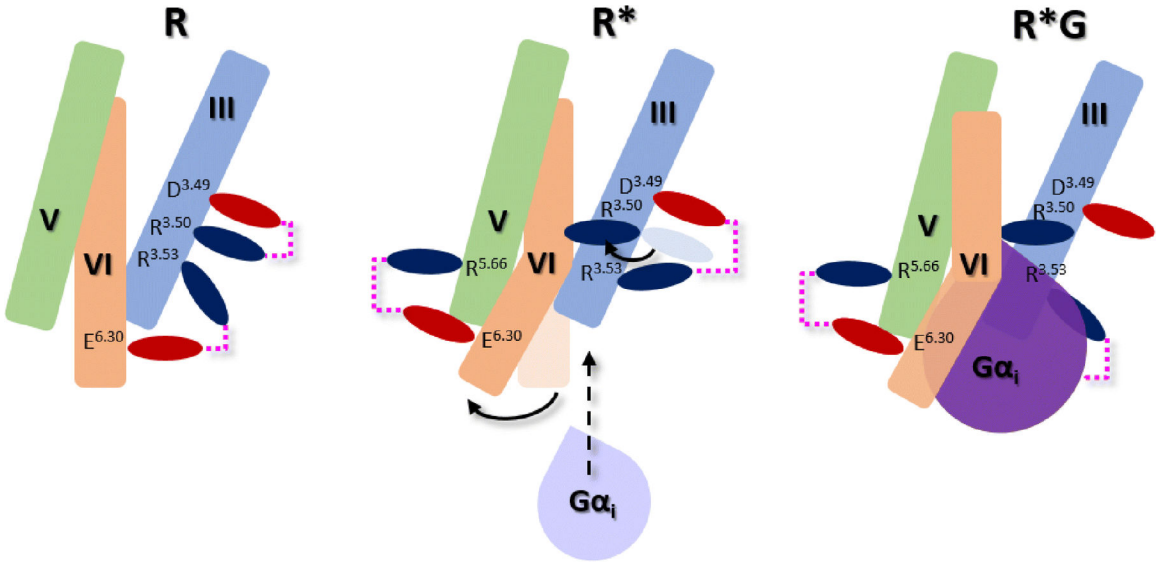

Figure 4.

Cartoon representation of interactions important for maintaining the three states of the WT hA_3AR. Positively and negatively charged residues are represented as blue and red ovals, respectively. Salt bridges are depicted as magenta dashed lines.

Table 1.

Persistency (% simulation time) of salt-bridges expressed as the average percent simulated time in which the N-O distance of oppositely charged residues was < 4Å calculated for each model/mutant over three independent trajectories. Model legend: R: HM derived from the A_{2A}^{4EIY} template; R*: HM derived from the A_{2A}^{5G53} -A_{2A}^{4EIY} template. Only salt-bridges occurring in TM domains and persisting for more than 40% of the simulation time at least in one model/mutant are reported. Standard deviation is reported in parenthesis. Detailed per replicate data are reported in Table S4.

	Inactive (R)				Active (R*)			
Salt bridge	**WT**	**R108K**	**R108A**	**A229E**	**WT**	**R108K**	**R108A**	**A229E**
Persistent irrespective of receptor state								
D175$^{5.30}$-R173$^{5.34}$,[a]	98 (1)	99 (0)	99 (0)	61 (30)	93 (11)	97 (4)	88 (20)	95 (4)
D199$^{5.60}$-K1 13$^{3.55}$[a]	74 (22)	85 (13)	42 (23)	94 (3)	85 (5)	94 (8)	89 (5)	90 (12)
Persistent in the inactive state (R)								
D107$^{3.49}$-R/K108$^{3.50}$,[b]	54 (22)	2 (2)	NA	34 (9)	ND	ND	NA	ND
E225$^{6.30}$-R/K108$^{3.50}$	3 (1)	86 (12)	NA	ND	ND	ND	NA	ND
E229$^{6.34}$-R111$^{3.53}$	NA	NA	NA	72 (26)	NA	NA	NA	ND
E225$^{6.30}$-R111$^{3.53}$,[b]	76 (12)	27 (21)	21 (15)	1 (0)	ND	ND	ND	ND
Persistent in the active state (R)*								
D107$^{3.49}$-R111$^{3.53}$,[c]	ND	26 (46)	38 (48)	ND	69 (14)	92 (1)	96 (5)	85 (23)
E225$^{6.30}$-R205$^{5.66}$[c]	ND	ND	ND	ND	82 (10)	89 (9)	55 (32)	75 (8)
E229$^{6.34}$-K230$^{6.35}$	NA	NA	NA	ND	ND	ND	ND	44 (4)

[a] Intrinsic feature.

[b] Inactive state signature.

[c] Active state signature.

NA: not applicable. ND: not detected.

Table 2.

Average Cα RMSD and RMSF values [Å]. Standard deviation is reported in parenthesis. Trajectories selected for visualization are in bold. Outliers in this table and in Tables S4 – S6 arise from the different initial seeds (random atom velocities) assigned to each simulation, that can cause the systems to evolve towards slightly different energy states representing local minima. As we simulated using classical MD, the systems cannot escape these meta-stable states as no energy boost is applied. The outliers are an indication of the roughness of the potential energy surface along the selected reaction coordinate. As we simulated HMs, they are not unexpected, as local adjustments in sidechain and loop orientation might allow the system to evolve differently from the initial state.

	R				**R***			
	WT	**R108K**	**R108A**	**A229E**	**WT**	**R108K**	**R108A**	**A229E**
				RMSD				
Run1	2.63 (0.62)	4.04 (0.83)	2.91 (0.81)	3.88 (0.89)	**3.40 (0.56)**	3.50 (0.76)	2.84 (0.55)	2.84 (0.80)
Run2	2.52 (0.48)	**3.18 (0.63)**	3.56 (0.75)	3.97 (0.70)	3.73 (0.75)	3.15 (0.57)	3.16 (0.80)	**2.40 (0.47)**
Run3	**1.92 (0.20)**	3.37 (0.51)	**2.42 (0.34)**	**3.00 (0.58)**	3.56 (0.66)	**2.40 (0.47)**	**2.59 (0.30)**	2.55 (0.33)
				RMSF				
Run1	1.74 (0.32)	1.96 (0.43)	1.95 (0.32)	2.00 (0.37)	**1.96 (0.32)**	1.80 (0.64)	2.07 (0.45)	2.08 (0.69)
Run2	1.64 (0.31)	**1.95 (0.49)**	1.98 (0.55)	1.98 (0.39)	2.05 (0.29)	2.12 (0.79)	1.88 (0.31)	**1.53 (0.53)**
Run3	**1.27 (0.16)**	1.74 (0.34)	**1.48 (0.21)**	**1.85 (0.23)**	1.63 (0.46)	**1.68 (0.29)**	**1.67 (0.28)**	1.65 (0.37)

Table 3.

Conformation of W243 and presence of sodium ions and water molecules in the TM bundle. Percent simulated time in which the conserved W243$^{6.48}$ residue χ_1 and χ_2 values adopted either a *gauche (g)* or *trans (t)* conformation (see Figure S6 for angles definitions and values). Percent simulated time in which a Na^+ ion was in proximity to E19$^{1.39}$ and/or D58$^{2.50}$ side chain (Na^+-side chain distance < 4Å). Number of water molecules (NumWat) present within the TM bundle. All values represent averages calculated over three independent trajectories. Detailed per replicate data are reported in Table S5–S7.

	Inactive (R)									Active (R*)								
	W243 χ_1			W243 χ_2			Na^+		NumWat	W243 χ_1			W243 χ_2			Na^+		NumWat
Mutation	***g*+**	***t***	***g*⁻**	***g*+**	**t**	***g*⁻**	**E19**	**D58**		***g*+**	***t***	***g*⁻**	***g*+**	***t***	**g⁻**	**E19**	**D58**	
WT	0	**75**	25	34	3	**64**	70	61	317±24	0	0	**100**	0	0	**100**	79	0	374±20
R108K	0	32	**68**	5	4	**91**	19	91	351±25	0	0	**100**	0	0	**100**	97	0	410±24
R108A	0	**81**	19	2	4	**94**	36	96	337±3	0	20	**80**	0	13	**87**	84	0	409±22
A229E	0	**62**	38	29	3	**69**	71	54	359±21	0	0	**100**	0	0	**100**	99	0	398±22

Table 4.

Persistency of salt-bridges at the interface between the hA_3AR and the $G\alpha_i$ protein expressed as average percent total simulation time (calculated over three independent trajectories) in which the N-O distance of oppositely charged residues was < 4Å. Standard deviation is reported in parenthesis. Detailed per replicate data are reported in Table S4.

	R*G			
Salt bridge	**WT**	**R108K**	**R108A**	**A229E**
D341[a]-K207$^{5.68}$	91 (8)	93 (7)	92 (10)	91 (9)
D193[a]-R120	45 (36)	66 (28)	58 (29)	31 (46)
E318[a]-K207$^{5.68}$	8 (13)	57 (39)	77 (27)	3 (5)[b]
E33[a]-K119^{IL2}	34 (34)	57 (31)	57 (22)	45 (19)
E33[a]-R120^{IL2}	24 (41)	33 (38)	35 (31)	68 (53)
D315[a]-K224$^{6.29}$	32 (31)	ND	62 (15)	ND

[a]Residue of the $G\alpha_i$ subunit.

[b]E318-R224$^{6.29}$: 16 (25)